Electronic Supplementary Material (ESI) for Nanoscale.
This journal is © The Royal Society of Chemistry 2023

Supporting Information: Reflective Dielectric Cavity Enhanced Emission from Hexagonal Boron Nitride Spin Defect Arrays

Xiao-Dong Zeng,[1,2] Yuan-Ze Yang,[1,2] Nai-Jie Guo,[1,2] Zhi-Peng Li,[1,2] Zhao-An Wang,[1,2] Lin-Ke Xie,[1,2] Shang Yu,[1,2] Yu Meng,[1,2] Qiang Li,[3,4] Jin-Shi Xu,[1,2,5] Wei Liu,[1,2,*] Yi-Tao Wang,[1,2,†] Jian-Shun Tang,[1,2,5,‡] Chuan-Feng Li,[1,2,5,§] and Guang-Can Guo[1,2,5]

[1]*CAS Key Laboratory of Quantum Information, University of Science and Technology of China, Hefei, Anhui 230026, China*

[2]*CAS Center For Excellence in Quantum Information and Quantum Physics, University of Science and Technology of China, Hefei, Anhui 230026, China*

[3]*Institute of Advanced Semiconductors and Zhejiang Provincial Key Laboratory of Power Semiconductor Materials and Devices, ZJU-Hangzhou Global Scientific and Technological Innovation Center, Hangzhou, Zhejiang 311200, China*

[4]*State Key Laboratory of Silicon Materials and Advanced Semiconductors and School of Materials Science and Engineering, Zhejiang University, Hangzhou 310027, China*

[5]*Hefei National Laboratory, University of Science and Technology of China, Hefei, Anhui 230088, China*

(Dated: August 27, 2023)

Contents

S1. Fluorescence intensities of V_B^- spin defects in hBN with different thicknesses. 3

S2. Supplementary for FDTD Simulation. 7

S3. Effect of implantation parameters on fluorescence intensity. 12

S4. Estimation of the density and yeild of V_B^- defect. 14

S5. Supplementary for ODMR data. 16

References 17

*Email: lw691225@ustc.edu.cn

†Email: yitao@ustc.edu.cn

‡Email: tjs@ustc.edu.cn

§Email: cfli@ustc.edu.cn

S1. Fluorescence intensities of V_B^- spin defects in hBN with different thicknesses.

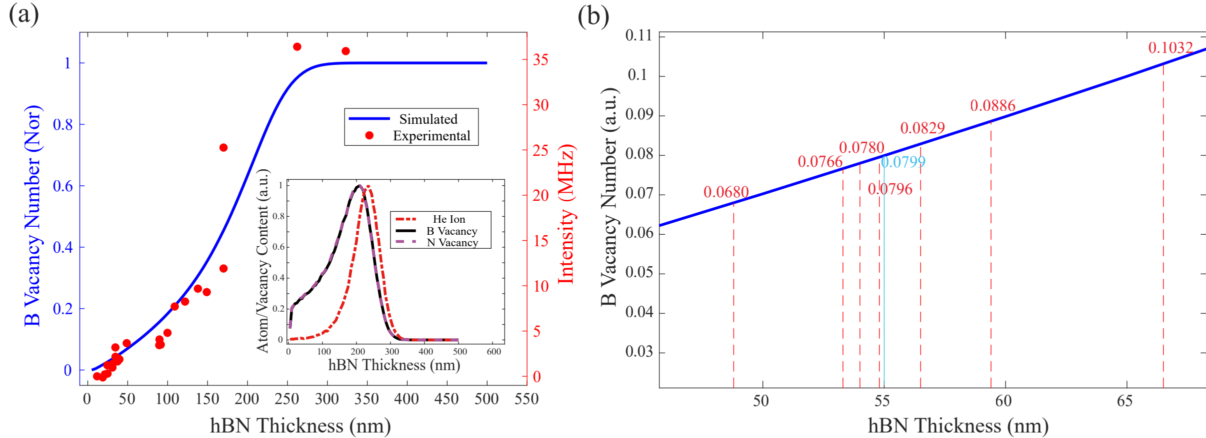

Fig. S1. (a) The red dots are the fluorescence intensities of V_B^- spin defects in hBN with different thicknesses on SiO_2/Si substrate. The V_B^- defects were generated by He^+ implantation with a dose of 1×10^{17} ions/cm^2, an energy of 30 keV and an implantation aperture of 100 nm, and the data were corrected by subtracting background fluorescence. The blue curve is the simulated relationship between the number of boron vacancies and the thickness of hBN, which is obtained by integrating the distribution curve of boron vacancy obtained by Stopping-and-Range-of-Ions-in-Matter (SRIM) simulation. Inset: Distribution of He ion, boron vacancy and nitride vacancy simulated by SRIM. (b) The relative number of boron vacancy in hBN with thickness near 55 nm.

The thickness of hBN has crucial effect on the number of defects generated by ion implantation under the same conditions. Here, we measured the emission intensity of generated V_B^- defects in hBN flakes with different thickness on SiO_2/Si substrates under the same ion implantation conditions (30-keV energy, 1×10^{17}-ions/cm^2 dose, 100-nm implantation aperture), where the thickness was measured by a profilometer (Dektak XT) (red dots in Fig. S1(a)). The data were corrected by subtracting background fluorescence. For the thin hBN (< 300 nm), the number of generated V_B^- defects is small and the measured fluorescence intensity is close to the background fluorescence intensity, resulting the negative data in Fig. S1(a). We also simulated the theoretical distribution of the boron vacancy with a depth created by 30-keV He^+ ions using Stopping-and-Range-of-Ions-in-Matter (SRIM) simulation (Fig. S1(a) inset). We simply assume that all the generated boron vacancies can form V_B^-

spin defects. By integrating the distribution curve of SRIM simulation and normalizing this derived integration result (blue curve in Fig. S1(a)), an approximate relationship between the number of V_B^- defects generated by ion implantation and the thickness of hBN is obtained. This is also the approximate relationship between emission intensity of V_B^- defects and hBN thickness after assuming that the emission intensity of V_B^- defects is proportional to the number. It is in good agreement with the experimental results. It should be noted that the effect of the substrate on ion implantation is ignored here.

To obtain rigorous enhancement factors of reflective dielectric cavity (RDC), we selected a group of hBN flakes with similar thicknesses ($\sim$ 55 nm) on different substrates to carry out the experiment. The chosen hBN thicknesses on different substrates were as follows: 48.8 nm@SiO_2/Si, 53.3 nm@0-nm RDC, 56.5 nm@20-nm RDC, 54.8 nm@50-nm RDC, 59.4 nm@80-nm RDC, 54 nm@110-nm RDC, and 66.5 nm@140-nm RDC. Using the same ion implantation parameters (30-keV energy, 1×10^{17}-ions/cm^2 dose, 100-nm implantation aperture), we generated 4×4 V_B^- defect arrays on these hBN flakes, and measured their emission intensity under the same excitation laser (4-mW 532-nm laser) (Fig. S2 and S3). We used the average intensity after subtracting background fluorescence as the emission intensity of each hBN flake, and further corrected the intensity by the simulation thickness-intensity model (see Table S1). After correction, the RDC structure can enhance the luminescence of V_B^- spin defects by 11 folds.

TABLE S1: Correction with thickness-intensity model.

	48.8 nm @ SiO_2/Si	53.3 nm @0-nm RDC	56.5 nm @20-nm RDC	54.8 nm @50-nm RDC	59.4 nm @80-nm RDC	54 nm @110-nm RDC	66.5 nm @140-nm RDC
Intensity /MHz (enhancement factor)	3.7(1.0)	22.3(6.0)	29.3(7.9)	25.5(6.9)	32.9(8.9)	22.7(6.1)	5.2(1.4)
Intensity /MHz (enhancement factor) after subtracting background fluorescence)	2.3(1.0)	22.0(9.6)	29.0(12.6)	25.2(11.0)	32.6(14.2)	22.4(9.7)	4.9(2.1)
Corrected intensity/MHz (enhancement factor)[a]	2.7(1.0)	22.9(8.5)	28.0(10.3)	25.3(9.4)	29.4(10.9)	22.9(8.5)	3.8(1.4)

[a] As shown in Fig. S1(b), the simulated relative values of the number of boron vacancies in different thicknesses of hBN are 0.0680 (48.8 nm), 0.0767 (53.3 nm), 0.0829 (56.5 nm), 0.0796 (54.8 nm), 0.0886 (59.4 nm), 0.0780 (54 nm), 0.1032 (66.5 nm) and 0.0799 (55 nm). The corrected intensities correspond to that of 55-nm hBN on different substrates converted from these simulated values.

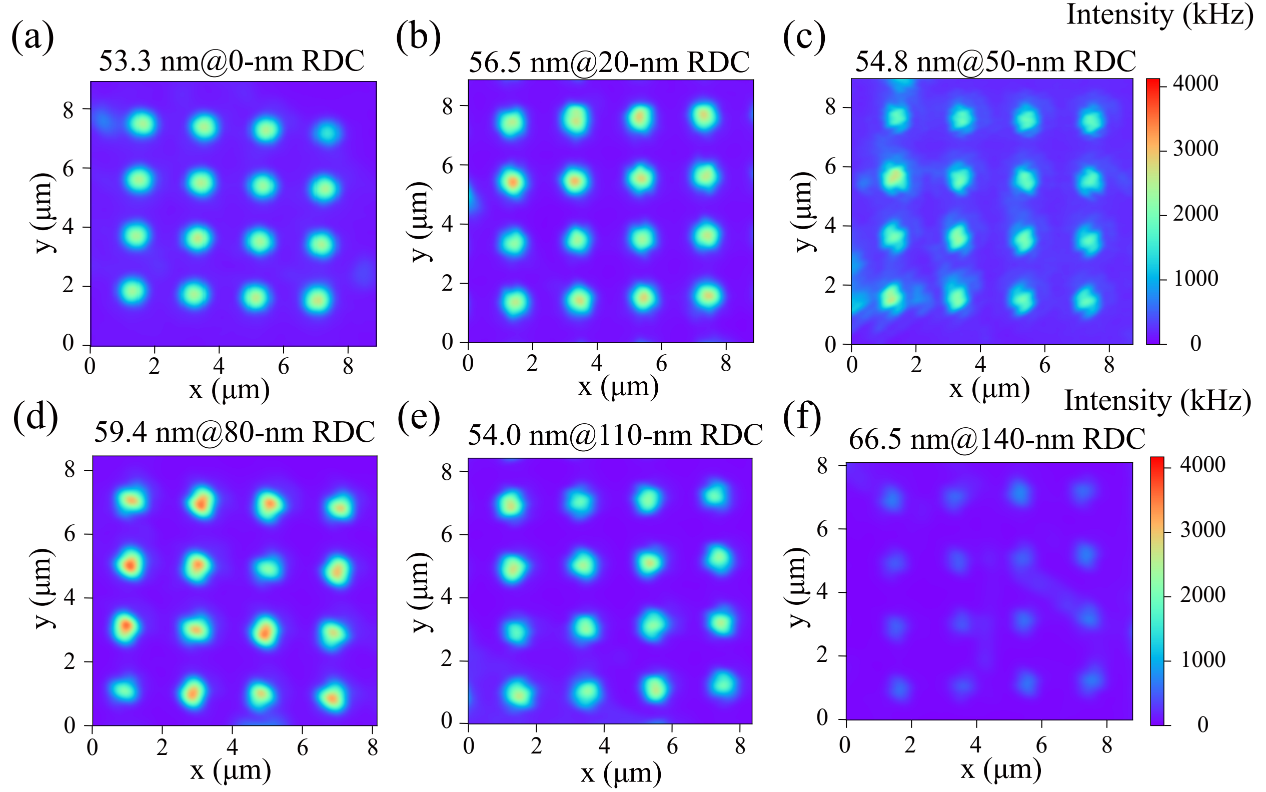

Fig. S2. Photoluminescence (PL) maps of hBN samples on different RDCs.

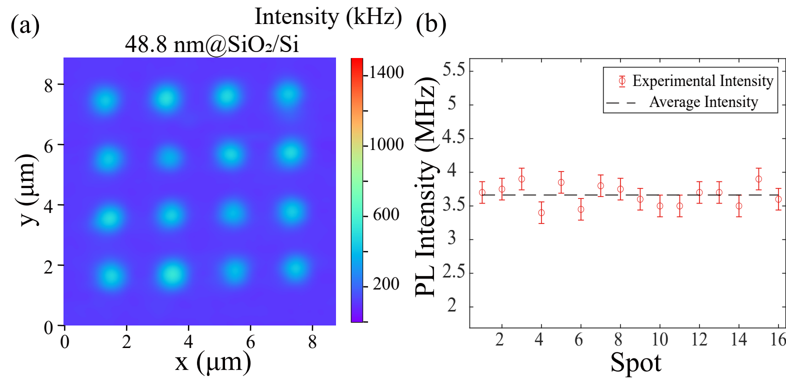

Fig. S3. (a) PL map of hBN sample (48.8 nm) on SiO_2/Si substrate. (b) Fluorescence intensity of different V_B^- defect spots in (a).

S2. Supplementary for FDTD Simulation.

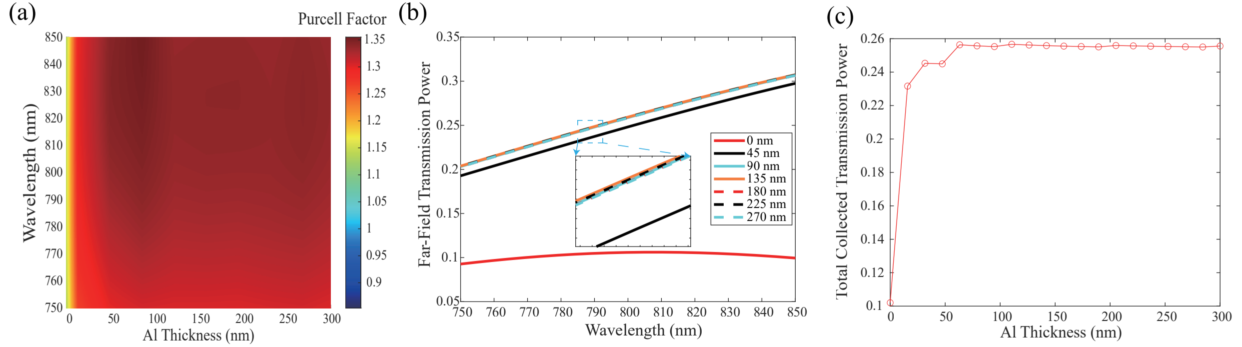

Fig. S4. Effect of aluminum (Al) reflector thickness on RDC enhancement. (a) The Purcell factor at different wavelengths as a function of Al reflector thickness. (b) The far-field transmission power of different Al reflector thicknesses as a function of wavelength of dipole source. (c) Total collected transmission power as a function of Al reflector thickness. In this simulation, the thickness of oxide dielectric layer (SiO_2) is set to 50 nm, the hBN thickness is set to 60 nm, and the dipole source is in-plane and set at the top of hBN.

There are many structural parameters that affect fluorescence enhancement of RDC, including metallic reflector thickness, dipole source orientation and position, hBN thickness, etc. Here, we used Finite-Difference-Time-Domain (FDTD) to simulate the effect of each parameter on Purcell factor and total collection transmission power.

The effect of Al reflector thickness on fluorescence enhancement of RDC is shown in Fig. S4. The Purcell factor and the total collection transmission power tend to saturate quickly. When Al reflector thickness is greater than 50 nm, the enhancement effect is basically the same. Therefore, we set the Al reflector thickness to 120 nm in the experiment. However, the Al layer is rapidly oxidized after production to form a dense oxide layer with a thickness of $\sim$ 5 nm, so in the next simulations, the Al reflector thickness is set to 115 nm with 5-nm Al_2O_3 on it.

The dipole source orientation also affects fluorescence enhancement of RDC. As shown in Fig. S5, while the in-plane orientation exhibits the highest Purcell enhancement factor for RDC, the collection efficiency compared to the out-of-plane orientation is weaker. Finally, the overall enhancement is optimal for the vertical orientation. Fröch *et al.* [1] investigated

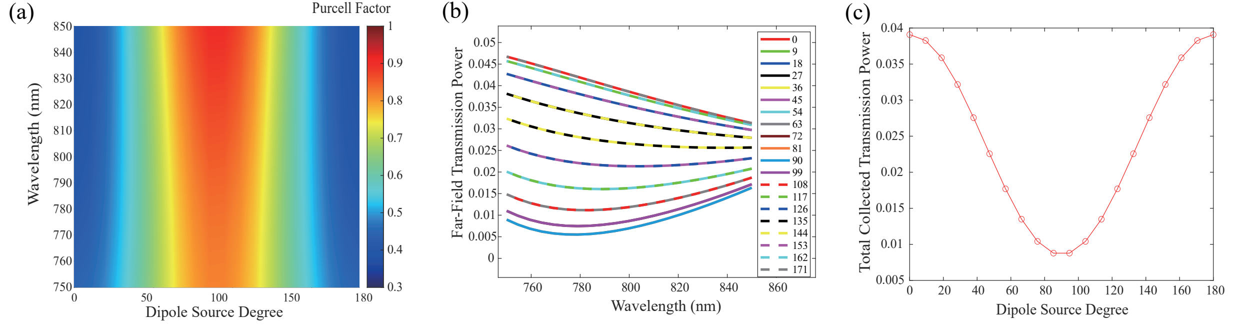

Fig. S5. Effect of dipole source orientation on RDC enhancement. (a) The Purcell factor at different wavelengths as a function of dipole source orientation. (b) The far-field transmission power of different dipole source orientations as a function of wavelength. (c) Total collected transmission power as a function of dipole source orientation. In this simulation, the thickness of oxide dielectric layer (SiO_2) is set to 50 nm, the hBN thickness is set to 100 nm, the Al reflector thickness is set to 115 nm with 5-nm Al_2O_3 on it, and the dipole source is set at the middle of hBN. 0° indicates that the dipole source is parallel to the *c*-aixs of hBN (vertical), and 90° indicates that the dipole source is perpendicular to the *c*-aixs of hBN (in-plane).

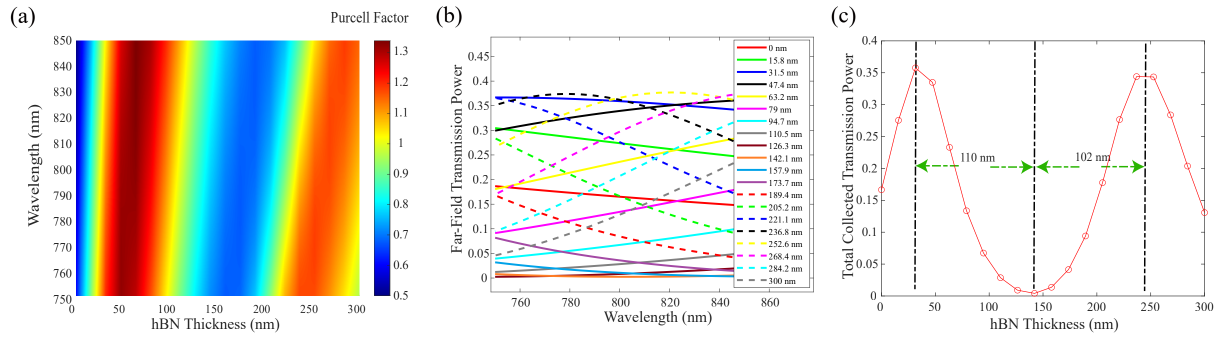

Fig. S6. Effect of hBN thickness on RDC enhancement. (a) The Purcell factor at different wavelengths as a function of hBN thickness. (b) The far-field transmission power of different hBN thicknesses as a function of wavelengths of dipole source. (c) Total collected transmission power as a function of hBN thickness. In this simulation, the thickness of oxide dielectric layer (SiO_2) is set to 50 nm, the Al reflector thickness is set to 115 nm with 5-nm Al_2O_3 on it, and the dipole source is in-plane and set at the top of hBN.

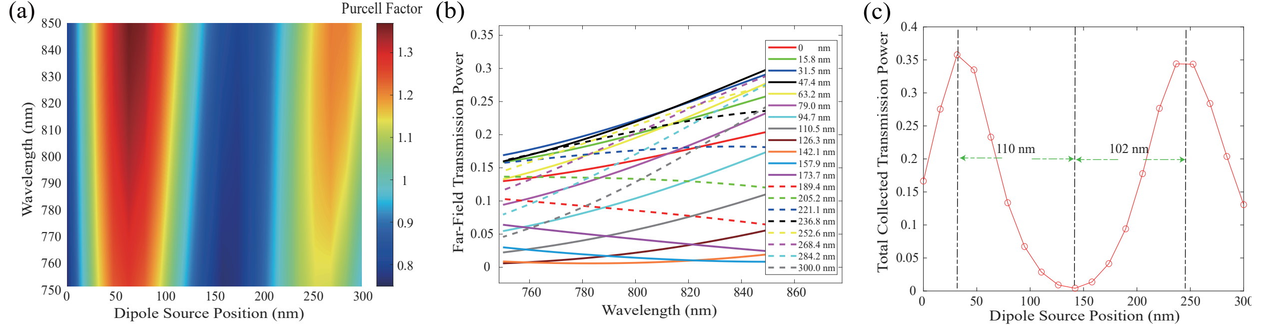

Fig. S7. Effect of dipole source position in hBN on RDC enhancement. (a) The Purcell factor at different wavelengths as a function of the position of dipole source. (b) The far-field transmission power of different dipole source positions as a function of wavelengths of dipole source. (c) Total collected transmission power as a function of dipole source position. In this simulation, the thickness of oxide dielectric layer (SiO_2) is set to 50 nm, the thickness of Al reflector is set to 115 nm with 5-nm Al_2O_3 on it, the thickness of hBN is set to 300 nm, and the dipole source is in-plane. The dipole source position refers to the distance between the dipole source and the lower surface of hBN flake.

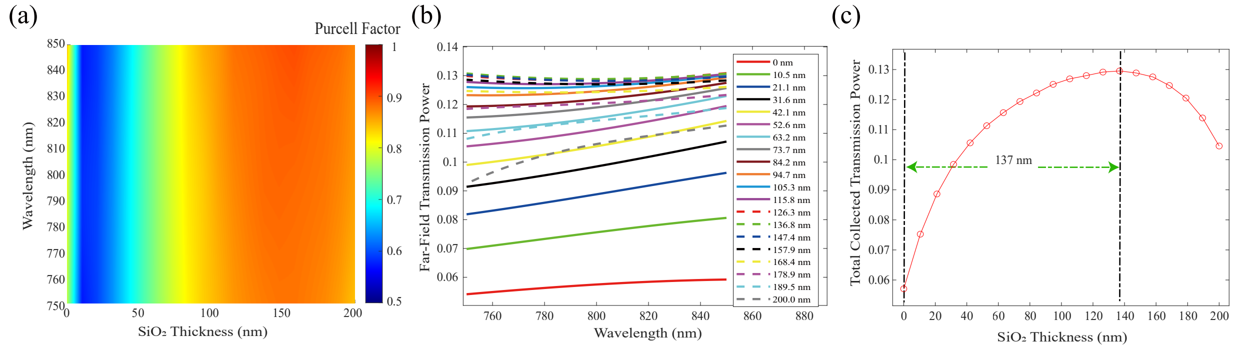

Fig. S8. Effect of the thickness of SiO_2 on RDC enhancement. (a) The Purcell factor at different wavelengths as a function of SiO_2 thickness. (b) The far-field transmission power of different SiO_2 thicknesses as a function of wavelengths of dipole source. (c) Total collected transmission power as a function of SiO_2 thickness. In this simulation, the thickness of hBN is set to 100 nm, the thickness of Al reflector is set to 115 nm with 5-nm Al_2O_3 on it, and the dipole source is in-plane and set at the bottom of hBN.

the dipole orientation of V_B^- and confirmed that it is in-plane, so we set the dipole sources all in-plane.

As a reflective dielectric cavity, the total dielectric layer thickness between the dipole source and the metal reflector plays a key role in the fluorescence enhancement. In addition to the SiO_2 dielectric layer ($n_{SiO_2} = 1.45$) we used to adjust the fluorescence enhancement of RDC already discussed in the main text, hBN as a dielectric layer with a larger refractive index ($n_{hBN} = 2$) also needs to be considered. As shown in Fig. S6, we set the dipole source at the top of hBN, and varied the thickness of hBN to explore its effect on the enhancement effect. Meanwhile, we also explored the effect of dipole source position in hBN on fluorescence enhancement of RDC by varying the distance of dipole source to the lower surface of hBN (Fig. S7). Comparing these two results, we can find that the enhancement effect curve of varying the position of the dipole source is very close to that of varying the thickness of hBN. Therefore, we believe that it is mainly the hBN below the dipole source affects the effect enhancement. In addition, it is evident that the reflective dielectric cavity is more sensitive to the thickness of hBN compared to SiO_2 (Fig. S8).

Considering the discussions above, we used the settings of multiple dipole sources in 55-nm hBN for the main sumulation (Fig. 3 in the main text). All dipole sources are in-plane. To obtain the position of dipole sources, we re-simulated the distribution of boron vacancy by SRIM taking the substrate structure into account (Fig. S9(a,b)). We found that after the He^+ enters the substrate through hBN, atoms in the substrate (such as Si) will be sputtered into hBN, quenching V_B^- fluorescence [2]. According to the result in Fig. S9(b), we assume that there is no V_B^- defect in the 5-nm hBN close to the substrate. Therefore, after comprehensively considering the distribution of V_B^- defect and calculation time, we finally set 9, 8, 6, and 2 dipole sources at 50 nm, 30 nm, 10 nm and 0 nm from the hBN top surface, respectively (Fig. S9(c)). The simulation results are shown in Fig. 3 in the main text and Fig. S9(d).

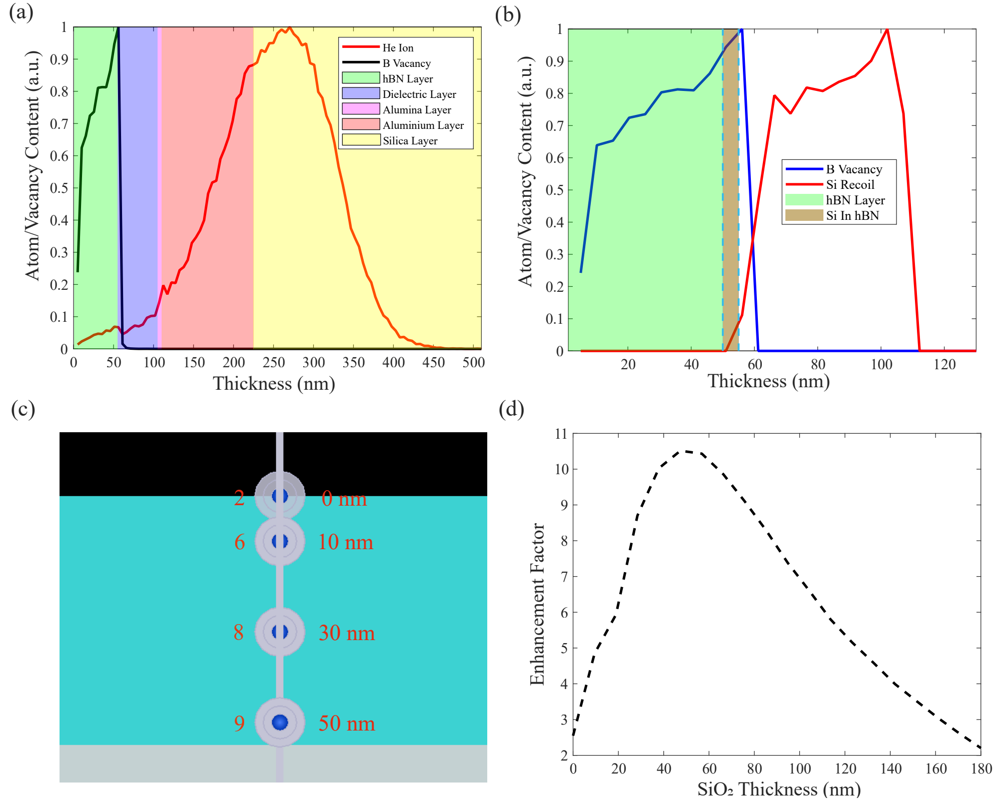

Fig. S9. Simulated settings of multiple dipole sources. (a) The distribution of He ion and boron vacancy. In this SRIM simulation, the hBN thickness is 55 nm, the substrate is 50-nm RDC, and the ion implantation energy is 30 keV. (b) The distribution of boron vacancy and the sputtering Si recoil. (c) Simulated settings of multiple dipole sources based on SRIM distribution of boron vacancy. (d) The simulated enhancement factor with different SiO_2 thicknesses based on the settings in (c).

S3. Effect of implantation parameters on fluorescence intensity.

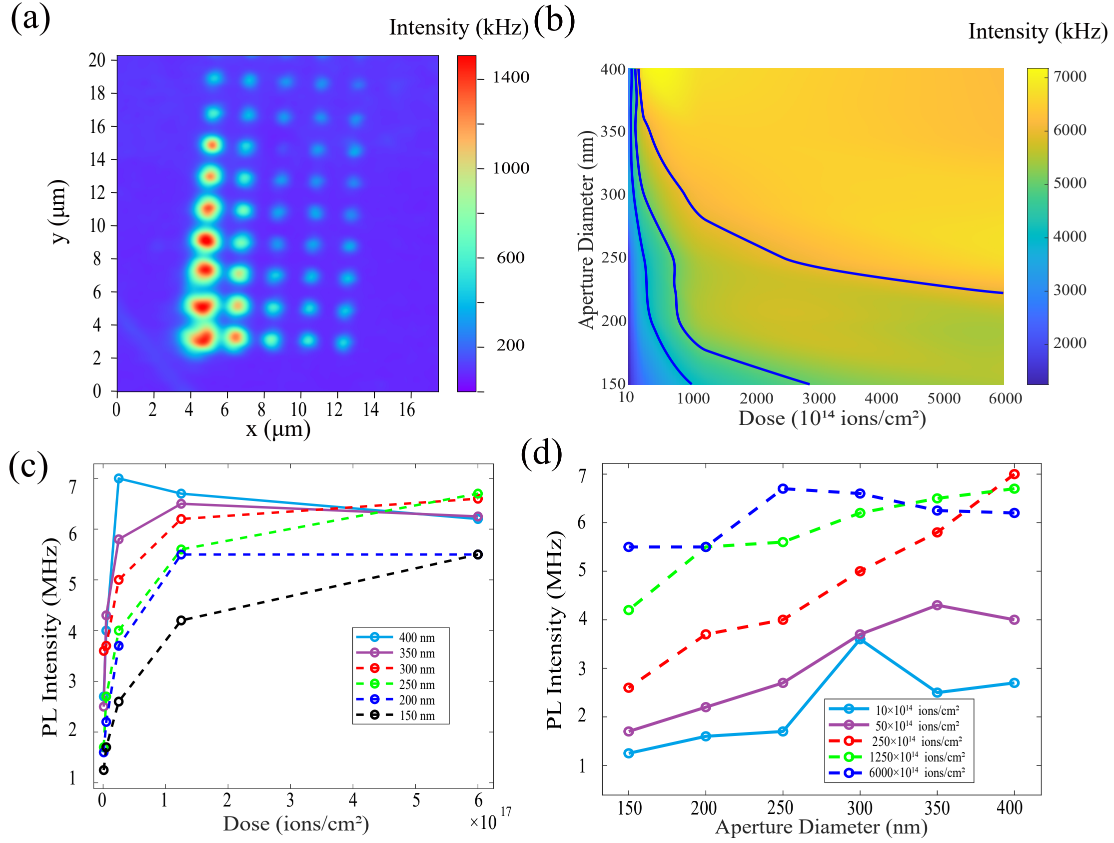

Fig. S10. (a) PL map of V_B^- spin defect arrays generated by different implantation doses and apertures. The implantation doses of each row are, from top to bottom, 1×10^{14}, $5{\times}10^{15}$, $2.5{\times}10^{16}$, $1.25{\times}10^{17}$, and $6{\times}10^{17}$ ions/cm^2, respectively. The implantation apertures of each column are, from right to left, 10 nm, 50 nm, 100 nm, 150 nm, 200 nm, 250 nm, 300 nm, 350 nm and 400 nm, respectively. (b) Two-dimensional contour plot of fluorescence intensity measured for different apertures and doses. The blue lines are the contour lines. (c) Fluorescence intensity of different implantation apertures as a function of implantation dose. (d) Fluorescence intensity of different implantation doses as a function of implantation aperture. All experiments were under 4-mW 532-nm laser excitation.

Fig. S10(a) shows the PL map of the V_B^- spin defect array generated by different implantation doses and apertures. With the implantation doses and implantation aperture increasing, the fluorescence intensity also increases. The fluorescence intensity saturates at an implantation dose of $\sim 1 \times 10^{17}$ ions/cm^2, and there is a linear relationship between the

implantation aperture and the fluorescence intensity because the implantation aperture is smaller than the laser spot ($d = 1.22\lambda/\mathrm{N.A.} = 720$ nm). Because of instrument limitations, we did not investigate the effect of implantation energy.

S4. Estimation of the density and yeild of V_B^- defect.

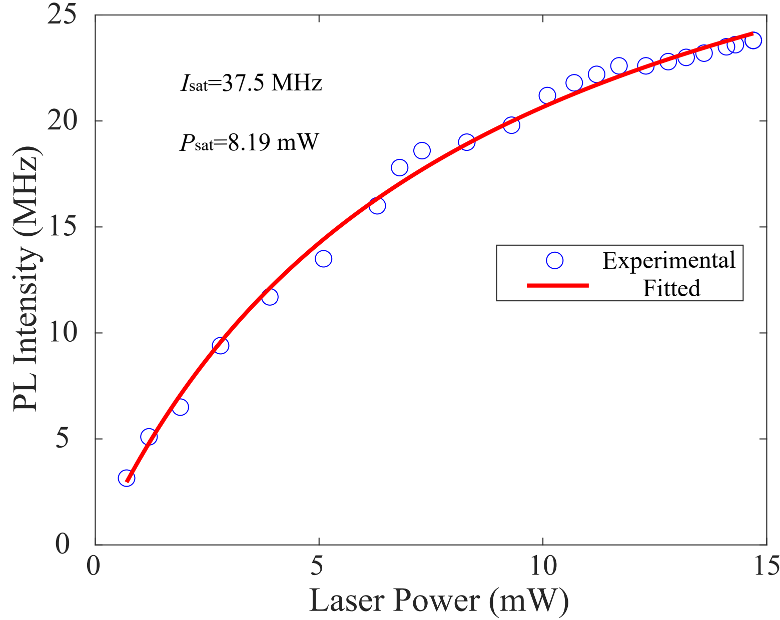

Fig. S11. Photoluminescence saturation curve of V_B^- defect ensemble on laser power. The fitting formula is $I(P) = I_{sat}P/(P_{sat} + P)$, where P represents the excitation power, I_{sat} and P_{sat} are fitting parameters. I_{sat} refers to the saturation radiative efficiency, while P_{sat} represents the saturation excitation power.

Due to the low quantum efficiency of V_B^- spin defects, it remains challenging to accurately count the defect density at the single defect level. However, here we can consider using the number of photons generated by picosecond pulse laser excitation as an approximate estimation of the order of magnitude of V_B^- spin defects. We can also estimate the yield of V_B^- spin defects per ion by ion implantation. The picosecond pulse laser operates at an extremely high pulse rate (78 MHz), so each pulse can be regarded as only exciting each defect once, allowing for the emission of at most one photon per defect in a single excitation. When the number of excited photons in the pump pulse exceeds the number of defects, we assume that the measured number of photoluminescence corresponds to the minimum number of defects. Based on these assumptions, we have previously made estimations of defect generation probability in our research group [3]. Taking certain losses into account, the number of V_B^- defects in a spot is estimated using the following equation:

$$n_{\text{defect}} = \frac{I_{\text{sat}}}{\eta N} \times \frac{D^2}{d^2} \quad (1)$$

where I_{sat} (37.5 MHz) is the saturated count, $\eta(\sim 0.8\%)$ is the loss coefficient (including objective collection efficiency (28%) and coupling efficiency on the collection side (10%), filter and BS transmission efficiency (40%), and detection efficiency of single photon detector (70%)), D is the diameter of the V_B^- spin defect ensemble distribution (1100 nm, see Fig. S12), d (720 nm) is the diameter of laser spot, and N (78 MHz) is pulse number per second. Therefore, the estimated lower limit of the number of V_B^- defects is 140.

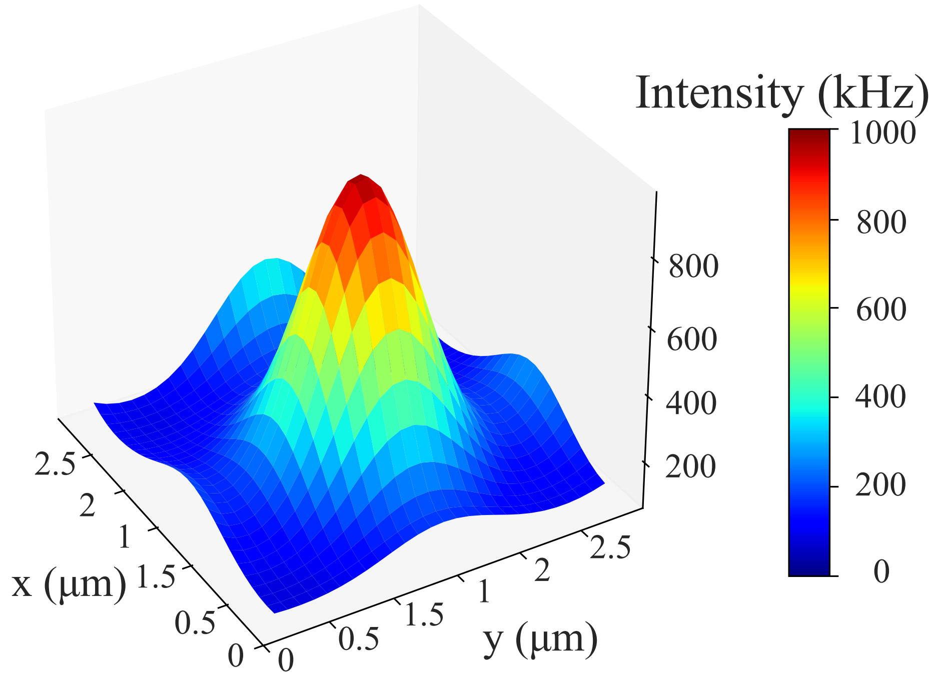

Fig. S12. Fluorescence intensity distribution of a V_B^- defect spot.

After dividing by the number of He^+ implanted in each spot, we can estimate the generation yield. Specifically,

$$yield = \frac{n_{\text{defect}}}{F \times \pi \times (d'/2)^2} \quad (2)$$

where F (1×10^{17} ions/cm^2) is implantation dose, d' (100 nm) is the diameter of the implantation aperture. The estimated lower bound of the generation yield is $\sim 2 \times 10^{-5}\%$.

S5. Supplementary for ODMR data.

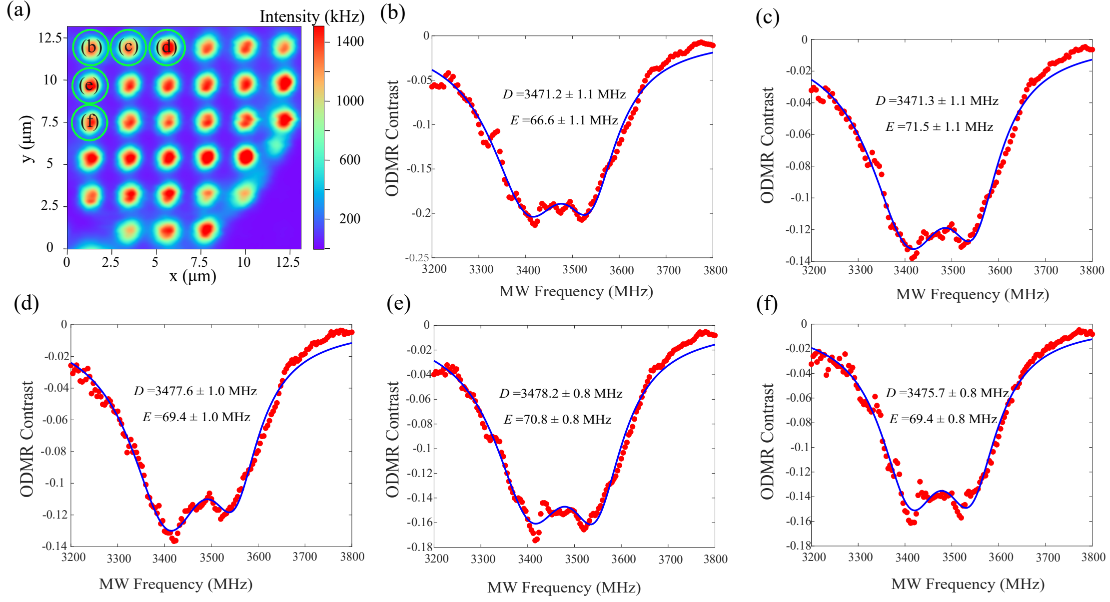

Fig. S13. (a) PL map of the V_B^- spin defect array on 50-nm RDC (corresponding to Fig. 2(b) in the main text). (b-f) ODMR spectra and theoretical two-Lorentzian fits (blue lines) of five V_B^- defect spots, corresponding to green circles in (a).

For V_B^- spin defect array on 50-nm RDC, we randomly selected five spots to measure the ODMR signal, as shown in Fig. S13. The contrasts are all higher than 14%, and the maximum can reach 21% (Fig. S14(b)).

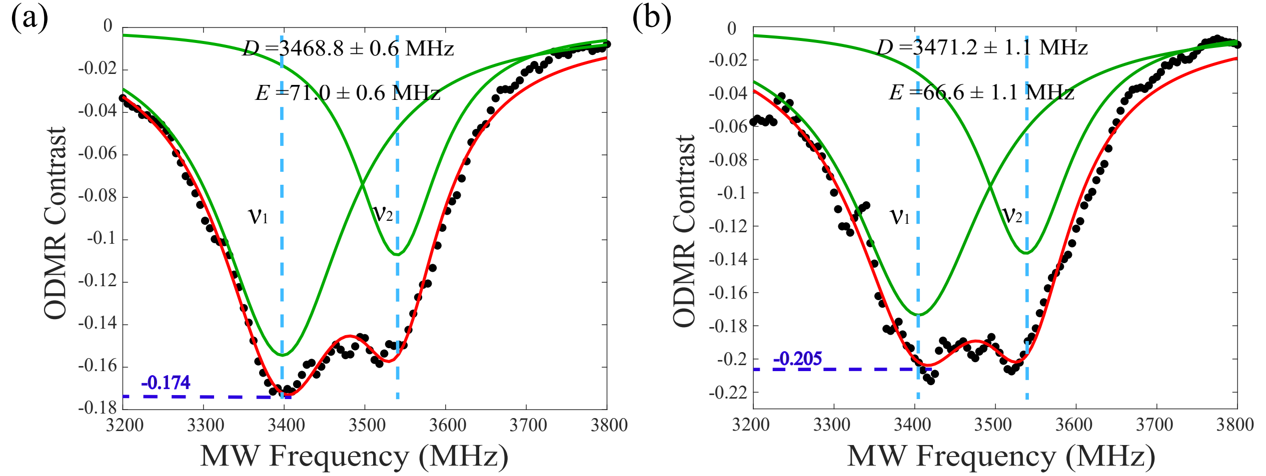

Fig. S14. (a) ODMR spectrum and theoretical two-Lorentzian fit corresponds to the spot in Fig. 4(b). The maximum contrast is 17%. (b) ODMR spectrum and theoretical two-Lorentzian fit corresponds to the spot in Fig. S13(b). The maximum contrast is 21%.

---

[1] J. E. Fröch, L. Spencer, M. Kianinia, D. Totonjian, M. Nguyen, V. Dyakonov, M. Toth, S. Kim and I. Aharonovich, Coupling spin defects in hexagonal boron nitride to monolithic bullseys cavities, *Nano Lett.*, 2021, **21**, 6549-6555.

[2] M. Hennessey, B. Whitefield, M. Kianinia, J. A. Scott, I. Aharonovich and M. Toth, Framework for engineering of spin defects in hexagonal boron nitride by focused ion beams, arXiv:2303.06784, 2023.

[3] N.-J. Guo, W. Liu, Z.-P. Li, Y.-Z. Yang, S. Yu, Y. Meng, Z.-A. Wang, X.-D. Zeng, F.-F. Yan, Q. Li, J.-F. Wang, J.-S. Xu, Y.-T. Wang, J.-S. Tang, C.-F. Li and G.-C. Guo, Generation of spin defects by ion implantation in hexagonal boron nitride, *ACS Omega*, 2022, **7**, 1733-1739.